Permafrost-related hiatuses in stalagmites: Evaluating the potential for reconstruction of carbon cycle dynamics

Franziska A. Lechleitner[1]*, Andrew Mason[1], Sebastian F. M. Breitenbach[2], Anton Vaks[3], Negar Haghipour[4,5], Gideon M. Henderson[1]

1) Department of Earth Sciences, University of Oxford, South Parks Road, Oxford OX1 3AN, UK
2) Institute for Geology, Mineralogy, & Geophysics, Ruhr-Universität Bochum, Universitätsstrasse 150, Bochum, Germany
3) Geological Survey of Israel, Malkei-Israel Street 30, Jerusalem, Israel
4) Department of Earth Sciences, ETH Zurich, Sonneggstrasse 5, 8092 Zürich, Switzerland
5) Laboratory of Ion Beam Physics, Department of Physics, ETH Zurich, Otto-Stern-Weg 5, 8093 Zurich, Switzerland

*corresponding author: franziska.lechleitner@earth.ox.ac.uk

Keywords: permafrost; stalagmite/speleothem; Siberia; carbon cycle; radiocarbon; trace elements; U-Th dating

Abstract

Permafrost is widely present throughout the Northern Hemisphere high latitudes, and stores large amounts of carbon in the form of frozen soil organic matter. The response of permafrost regions to anthropogenic climate change remains uncertain, in part because of a lack of information on their response to past changes in global climate. Here we test the use of stalagmites from two caves in Siberia as a novel, precisely dated, and highly localised archive of past permafrost carbon cycle dynamics. Stalagmite growth at these sites is controlled by the presence/absence of permafrost above the cave over glacial-interglacial time scales. We target the transition layer between two subsequent growth phases (interglacials) and the interval directly following growth resumption after the last glacial in three stalagmites, as this is where a geochemical imprint of thaw-related processes in the frozen zone between surface and cave would be recorded. We apply a multi-proxy approach including carbon isotopes ($\delta^{13}C$ and ^{14}C)

and trace element concentrations, combined with petrographic analyses and high-resolution U-Th chronology. Our dataset indicates complex growth patterns and possible intervals of microbial colonisation of the stalagmite surface in the transition layers. High-resolution U-Th ages confirm that the transition layer is not a single, long growth hiatus, but rather a period of extremely slow or episodic growth phases, possibly during "skipped" interglacials. However, we find no conclusive evidence for a geochemical signature related to permafrost degradation and related local carbon cycle dynamics, which might be related to insufficient sensitivity of the archive for high-frequency processes and/or insufficient measurement resolution.

1. Introduction

Permafrost deposits cover over 20% of the Northern Hemisphere land surface and contain more than twice as much carbon as the pre-industrial atmosphere (Hugelius et al., 2014). The fate of this large reservoir of carbon under anthropogenic climate change remains uncertain (Schuur et al., 2015) and its non-linear responses might significantly impact calculated emission budgets (Gasser et al., 2019, 2018). Rising global temperatures could lead to widespread permafrost destabilisation and thawing, releasing carbon to the atmosphere and leading to a positive feedback in the climate system (Biskaborn et al., 2019; Comyn-Platt et al., 2018a, 2018b; Grosse et al., 2011). On the other hand, thawed permafrost terranes could also act as carbon sinks, e.g., through carbon accumulation in thermokarst lakes (Walter Anthony et al., 2014). Much of the uncertainty in the response of permafrost regions to climate warming stems from their spatial heterogeneities (Hjort et al., 2018; Hugelius et al., 2014), regional differences in the lability of soil organic matter (Kuhry et al., 2019), highly localised thawing processes (Walter Anthony et al., 2018), and relatively slow response relative to observational timescales. Reconstruction of past periods of permafrost thawing might help address these uncertainties, but little is known about permafrost stability and the fate of carbon in these systems in the past. Marine records from (sub-)polar regions provide information on permafrost stability and carbon fluxes on supra-regional scale (Tesi et al., 2016; Winterfeld et al., 2018), but cannot resolve local and continental processes. Basal radiocarbon (^{14}C) dates from peat and thermokarst lake basins can be useful to reconstruct local carbon cycle dynamics after permafrost degradation (Jones and Yu, 2010; Walter Anthony et al., 2014), but are limited in their temporal resolution and in their chronology.

Stalagmites from caves in permafrost regions could provide a novel archive of past local carbon cycle dynamics. They have the significant advantage of being amenable to high-precision dating with the U-Th method (Hellstrom, 2006; Richards and Dorale, 2003; van Calsteren and Thomas, 2006), and could provide high-resolution reconstructions of subsurface permafrost dynamics. Stalagmite growth is controlled by the availability of liquid water percolating through the soil, epikarst, and limestone massif. In permafrost regions, this means that stalagmite growth is only possible when the surface and rock above the cave are free of permafrost and cave air temperature is >0°C. In these environments, growth/no growth can be interpreted as a first-order response to climate forcing (Atkinson et al., 1978; Vaks et al., 2013; Wilcox et al., 2019). Dating stalagmite growth periods therefore can allow reconstruction of permafrost occurrence and the delay in the response of deep permafrost degradation to surface warming.

While in the majority of cases stalagmite growth is a primarily abiotic process, a growing body of research has shown evidence for microbial influence on carbonate precipitation in caves (Frisia et al., 2012; Jones, 2011; Pacton et al., 2013; Tisato et al., 2015). Biomediation of carbonate precipitation provides an alternative growth mechanism that is potentially decoupled from local hydrological conditions, and typically leads to specific morphologic, petrographic, and geochemical features in the deposited stalagmites (Frisia, 2015; Pacton et al., 2013; Tisato et al., 2015).

The potential of stalagmite geochemical proxies as tracers for permafrost carbon cycle processes remains largely untested. Carbon isotopes, i.e., stable carbon isotope ratios ($\delta^{13}C$) and radiocarbon (^{14}C), could hold information about changes in the surface carbon cycle and provide a diagnostic fingerprint of permafrost degradation. A disproportionately large input from rapidly degrading stored soil organic matter during and after thawing would lead to a shift in $\delta^{13}C$ towards more negative values in the percolating dripwater, due to fractionation from biological fixation in plants. At the same time, ^{14}C values of the carbon released from organic matter stored over extended periods would be lower due to previous ^{14}C decay. It remains unclear however, the extent to which such near-surface carbon cycle perturbations will be reflected in stalagmites, because complex processes related to carbonate dissolution/precipitation and karst hydrology (Bajo et al., 2017; Bergel et al., 2017; Columbu et al., 2019; Genty et al., 2001; Griffiths et al., 2012; Mühlinghaus et al., 2007) could mask the original isotopic signature derived from degrading permafrost. Trace elements, especially those

involved in the transport of organic matter through formation of organo-metal complexes, are another potentially sensitive proxy for permafrost degradation processes and local carbon cycle dynamics. Elements such as P, Mn, Cu, Zn, Pb, and U are well-established as proxies for surface productivity and soil activity (Borsato et al., 2007; Frisia et al., 2012; Hartland et al., 2012; Rutlidge et al., 2014), but have yet to be tested in a permafrost setting. Important questions that need to be resolved to confidently apply stalagmites for the reconstruction of permafrost carbon cycle dynamics include constraining the complexities of permafrost formation and destruction in karst settings (Žák et al., 2012), as well as understanding the role of deep permafrost for overall carbon release upon thawing (Schuur et al., 2015).

Here we use samples from two caves in the Siberian permafrost region to investigate the suitability of stalagmites as archives for high-frequency environmental changes related to permafrost thawing. Stalagmites from these caves have grown intermittently during interglacial periods of at least the last 500 thousand years (ka), when permafrost above the caves was absent (Vaks et al., 2013). Using a multi-proxy geochemical approach and petrographic analysis, we test whether signatures of degrading permafrost were recorded by the stalagmites during or immediately following growth resumption after the last deglaciation (~10 ka BP, where BP stands for 'before present' referring to 1950 CE). More generally, we also assess what information might be gained from high-resolution measurements across stalagmite growth hiatuses.

2. Study sites and samples

Okhotnichya Cave (N52°07'41", E105°29'11", 700 m above sea level, a.s.l.) is located about 83 km E-SE from the city of Irkutsk in southern Siberia and is in a region at present covered by sporadic patches of permafrost (Fig. 1). The cave developed in Cambrian stromatolithic limestone with basaltic dyke intrusions, and is covered by mixed deciduous and conifer forest. A large, steeply descending entrance hall leads to several systems of passages with average depths of 20–30 m below surface, with individual passages up to 25 m high (Bazarova et al., 2014; Vaks et al., 2013). Water seepage and actively growing speleothems can be found throughout the cave. Cave temperatures are seasonally constant, varying spatially in the large cave complex from 0 to 1°C, while outside air temperatures vary between seasonal extremes of +34°C and -38°C (three-year mean surface air temperature: -0.2°C; Vaks et al., 2013).

Botovskaya Cave (55°17’59”N, 105°19’46”E, 750 m a.s.l.) is the longest cave system in Russia (>69.5 km of explored passages to date). The cave is presently covered by sporadic permafrost less than 100 m thick (Fig. 1). Botovskaya Cave developed in Ordovician quartz-bearing limestone, bracketed by carbonate-rich sandstones, and is covered by sub-boreal taiga forest. The cave passages are located 40–130 m below the surface, and developed as a near-horizontal crisscross maze of tectonic fissures (Filippov, 2000). Active speleothem growth is today only found in the eastern parts of the cave. Cave air temperatures vary between 0°C and 1.9°C, compared to outside temperature averages of -28°C in January and +18°C in July (Vaks et al., 2013).

The boreal climate at both sites is characterized by annual precipitation of 400-500 mm/year and a positive water balance, thus speleothem growth is not limited by aridity. In both caves, speleothem growth during the last 500 ka is controlled by the occurrence of permafrost above the cave, with growth phases coinciding with permafrost-free interglacial conditions and growth interruptions during glacials (Vaks et al., 2013). The timing of growth phases established by Vaks et al. (2013) was modelled in that study by extrapolating the range of individual U-Th ages to take into account the distance of the samples from the hiatuses, and temporal averaging from sampling. While localised conditions will have an influence on the timing of growth in a single stalagmite, similar growth boundaries in several speleothems will yield information on the regional climate control on permafrost presence/absence. Thus, for the Holocene and Marine Isotope Stage 5.5 (MIS 5.5), growth boundaries of different speleothems were assumed to be the same age, if corresponding U-Th ages were within 2 sigma error of each other (Vaks et al., 2013). For older growth phases, no modelling was performed, but the notion that similar ages in different stalagmites reflect regional climate conditions still holds true.

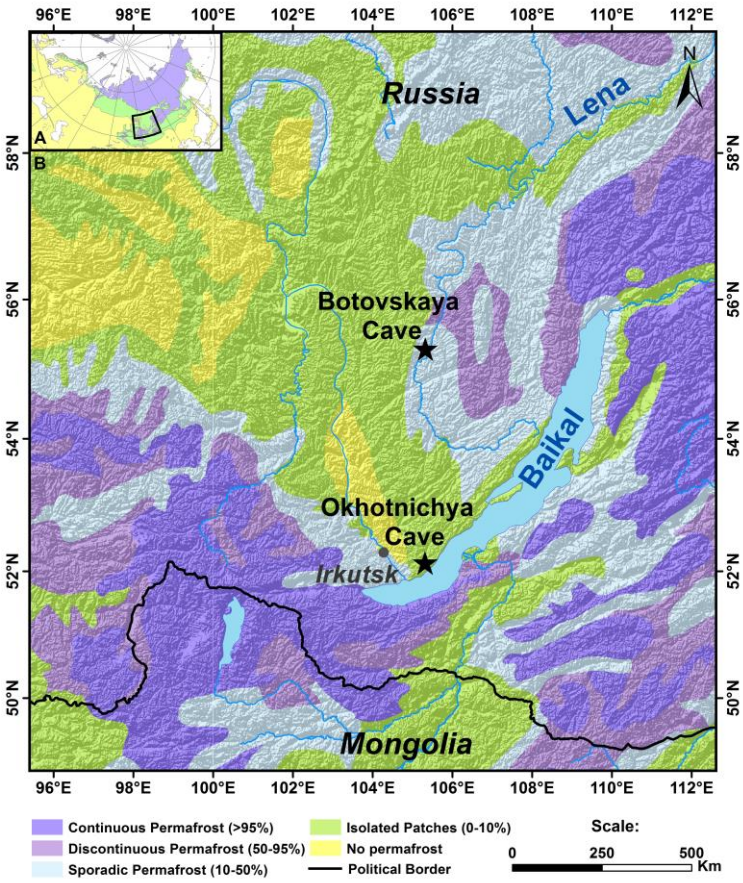

Fig 1: Map of the study region indicating occurrence of permafrost and the cave sites. Permafrost data is from the geocryological map of Russia and neighbouring republics (Williams and Warren, 1999; Yershov, 1991). The map was compiled using ESRI ArcGIS.

For this study, we selected three stalagmites previously U-Th dated by Vaks et al. (2013). All three stalagmites were actively growing when collected.

- Stalagmite SOP-20 was collected from the deep part of Okhotnichya Cave (~ 200 m from the entrance) in 2008. It is a relatively large stalagmite (~30 cm wide, 20 cm tall), and U-Th dating identified three main growth phases: the base of the stalagmite is beyond the dating limit of the U-Th method (>550 ka BP), followed by a growth interval ending at 377±7 ka BP (end of MIS 11). The final growth interval covers the Holocene with an OxCal modelled growth start at 9.99 ka BP and ending at present (Vaks et al., 2013). The growth intervals are composed of dense brown calcite in the older phases and white calcite in the Holocene. Clearly visible, brown-reddish layers, up to 2 mm in thickness, demarcate the hiatus in growth between MIS 11 and Holocene (Figs. 2, 3).

- SOP-18 is a drill core taken from a stalagmite from Okhotnichya Cave in 2010, located close to SOP-20. The core is about 2 cm wide and 5 cm long, and covers the Holocene portion of the stalagmite (OxCal modelled growth between 9.99 ka BP and present; Vaks et al., 2013), and part of the previous interval, which as in SOP-20 coincides with the end of MIS 11 (346±9 ka BP). The stalagmite is very similar to SOP-20 in mineralogy and colouring, and the transition between the two growth phases is again clearly visible as a mm-thick brown-reddish layer (Figs. 2, 4).
- Stalagmite SB-pk7497 was collected from the deepest, easternmost passages of Botovskaya Cave in 2010. The stalagmite is about 20 cm tall and 4 cm wide, and composed of aragonite. Two growth phases can be discerned, separated by a mm-thick brown transition layer. The top part of the stalagmite grew during the Holocene (OxCal modelled growth between 9.99 ka BP and present; Vaks et al., 2013), while the lower part grew during the last interglacial (122.71±0.64 – 118.83±0.52 ka BP) (Figs. 2, 5).

3. Methods

3.1. Sampling strategy

The stalagmites were available as cut slabs of the original samples. For petrographic analysis, thin sections were examined using a Nikon Labophot petrological microscope (Department of Earth Sciences, University of Oxford). Fluorescence microscopy was carried out on an Olympus FV3000 confocal microscope (Micron imaging facility, University of Oxford).

Samples for geochemical analysis were incrementally milled at 200 μm resolution over the interval between the two most recent growth phases, including the transition layers. Milling was carried out on a New-Wave/Mercantek micromill following a trench (5–10 mm wide, depending on the stalagmite) with a lateral cut drilled along the length of the trench prior to sampling (Fig. 6). This reduces sampling bias as incorporation of unsampled corners of the trench into subsequent samples is reduced. Moreover, 0.1 mm of sample were removed from the surface and discarded to minimise contamination. The sampling resolution was defined to be high enough to allow for the detection of meaningful geochemical trends in this very short growth interval, but also to yield enough material for all analyses to be performed on the same aliquot of powder,

minimising sampling bias from resampled trenches. Sampling trenches were milled from old to young material for SOP-20 and SOP-18, and from young to old for SB-pk7497. Milled carbonate powders were collected in acid-washed plastic tubes and stored before analysis.

3.2. Stable isotopes and trace elements

Stable carbon and oxygen isotope ratios ($\delta^{13}C$ and $\delta^{18}O$) were measured on sample aliquots (~50 μg $CaCO_3$) on a Delta V Advance isotope ratio mass spectrometer (IRMS) fitted with a Kiel IV carbonate device at the Department of Earth Sciences, University of Oxford, following the method described in Day and Henderson (2011). Stable isotope ratios are expressed in per mil (‰) relative to the international Vienna Pee Dee Belemnite (VPDB) standard, and the external error is assessed through repeated measurements of the standards NBS-18 and NBS-19 (1σ uncertainty 0.02‰ for $\delta^{13}C$ and 0.05‰ $\delta^{18}O$).

Trace element concentrations (Mg, P, Mn, Co, Ni, Cu, Zn, Sr, Cd, Ba, Pb, Th, U) were measured on a second aliquot of each powder (~50 μg $CaCO_3$) using a Nexion 350D quadrupole ICP-MS at the Department of Earth Sciences, University of Oxford. Samples were dissolved in 2% HNO_3 and analysed at 1 ppm Ca, concentration matched to within 10%. The ICP-MS was coupled with an ESI prepFAST autodiluter autosampler, which automated the preparation of each calibration standard and internal standard addition. Elemental concentrations were calculated by linear regression from the calibration curves where the correlation coefficients were required to be greater than 0.999. The elements Rh and In were used as internal standards and quality control standards were measured as dilutions from a separate standard stock (produced by CPAchem Ltd. and distributed by Qmx Laboratories). The measurement uncertainty was quantified using a secondary standard interspersed repeatedly during sample analysis (reported as 2 standard deviations).

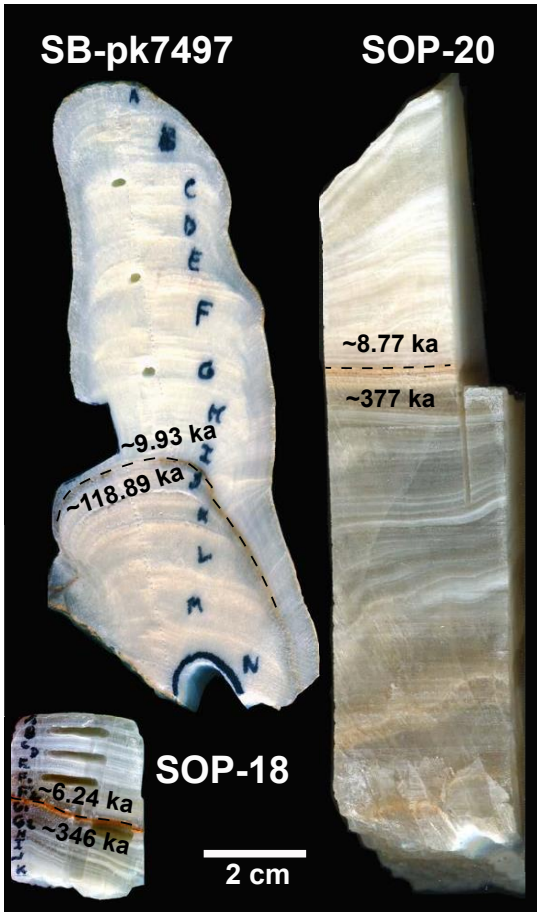

Fig 2: Stalagmites used in this study (SOP-20: cut piece of the stalagmite, SOP-18: drill core from the stalagmite top, SB-pk7497). Growth interruptions (transition layers) are marked by dashed lines, and the time elapsed between the main growth phases is indicated (as resulting from U-Th dating by Vaks et al., 2013).

3.3. U-Th dating

To pinpoint the exact location of the growth interruption in stalagmite SOP-20, aliquots from eight of the milled high-resolution samples were used for U-Th dating. To obtain enough material for analysis, a second track was milled next to the first one, and U concentrations were measured by ICP-MS so that patterns could be matched with those from the first track to correct for any depth bias (Supplementary table 1).

The samples were spiked with a mixed ^{229}Th-^{236}U spike, dissolved in concentrated HCl and refluxed on a hotplate overnight, before proceeding to U and Th separation via column chemistry. An extended wash protocol was applied to the columns before adding the samples, to minimise the blank contribution given the small sample sizes (between 4 and 9.7 mg $CaCO_3$). The U fraction was collected directly, while the Th fraction was taken through a second chemistry after conversion of the HCl to nitrate.

Measurement of U and Th was performed on a Nu Instrument Multi Collector Inductively Coupled Mass Spectrometer (MC-ICP-MS) at the Department of Earth Sciences, University of Oxford. U was measured using Faraday cups for ^{238}U, ^{236}U, and ^{235}U, and an ion-counter for ^{234}U, and abundance sensitivity was corrected based on half-mass dynamic measurements at 236.5, 235.5, 234.5, and 233.5 on the ion-counter. For the Th measurement, Faraday cups were used for ^{238}U, ^{235}U, and ^{232}Th, and ion-counters for ^{230}Th and ^{229}Th, following the procedure of Mason and Henderson (2010). Instrumental memory was measured at the beginning and end of the measurement run, and corrected for. Correction for signal noise was obtained by normalising to the respective ^{235}U measurement in each step. Abundance sensitivity was corrected by half-mass dynamic measurements at 230.5, 229.5, and 228.5 on the ion-counter. Standard sample bracketing using CRM-145 for U, and two in-house Th standards allowed correction for machine biases (ion-counter gains and mass fractionation). All U and Th isotope ratios are reported as activity ratios in round brackets (e.g., ($^{234}U/^{238}U$)).

3.4. Radiocarbon analysis

For stalagmite SOP-20, ^{14}C was measured at the Oxford Radiocarbon Accelerator Unit, School of Archaeology, University of Oxford. Sample aliquots (~7-8 mg $CaCO_3$) were dissolved in 85% H_3PO_4 and the resulting CO_2 was collected in flame-sealed glass ampules (Brock et al., 2010). After determination of their $\delta^{13}C$ value on a Europa Scientific IRMS, the remaining gas was converted to graphite via iron-catalysed hydrogen reduction before measurement by Accelerator Mass Spectrometry (AMS). For stalagmites SOP-18 and SB-pk7497, ^{14}C was measured at the Laboratory for Ion Beam Physics at ETH Zurich, Switzerland, using a Gas Ion Source coupled to a MICADAS AMS (Fahrni et al., 2013; Synal et al., 2007). Carbonate powders are converted to CO_2 through the addition of 85% H_3PO_4, and the gas is directly injected in the ion source of the AMS. This method circumvents the graphitisation step and thus results in much smaller sample sizes needed (~0.8 mg $CaCO_3$), a great advantage given the limited sample volumes in this study.

Repeated measurements of standards (Oxalic acid II, NIST SRM 4990C and IAEA C-2 as a carbonate standard for samples run at ETH) and carbonate blanks (IAEA C-1) ensured quality control of all AMS measurements. The procedural blank was evaluated through measurements of powders milled from the ^{14}C-dead portion of SOP-20

following the same protocol as the samples. ^{14}C concentrations are reported as $F^{14}C$ values ('fraction modern') according to Reimer et al. (2004).

4. Results

4.1. Petrography of the transition layers

In both stalagmites from Okhotnichya Cave, SOP-20 and SOP-18, the main growth phases are characterised by compact columnar calcite fabrics, as shown by previous XRD measurements (Vaks et al., 2013). Evidence for dissolution/corrosion, secondary infillings, and some neomorphism (microsparite and/or mosaic fabrics; Frisia, 2015) of the calcite is apparent in isolated patches in the transition layer in both stalagmites (Figs. 3 and 4). In SOP-20, the transition layer itself is composed of a succession of three bands of dark, non-light-transmitting, and very finely laminated material, with two brief phases of clear calcite growth in-between (Fig. 3). Fluorescence microscopy reveals that the dark bands in SOP-20 strongly fluoresce in the 488 nm band (an indication of high organic content; van Beynen et al., 2001). The transition layer in stalagmite SOP-18 is similarly composed of two dark, non-light-transmitting and fluorescing layers with an interlaid band of clear calcite. The transition from the underlying calcite shows evidence for isolated dissolution/corrosion, second-generation infillings, and possibly neomorphism, which is also found at the transition into the Holocene growth phase (Fig. 4).

Stalagmite SB-pk7497 from Botovskaya Cave is characterised by aragonitic needle fabric (determined by XRD; Vaks et al., 2013). The transition layer is much less visible than in SOP-20 and SOP-18, and thin section microscopy reveals only a thin and irregular layer of dark material (Fig. 5). Interestingly, the interval immediately preceding the transition layer appears to have been altered, and the primary aragonite needles have been partially replaced by mosaic fabric calcite.

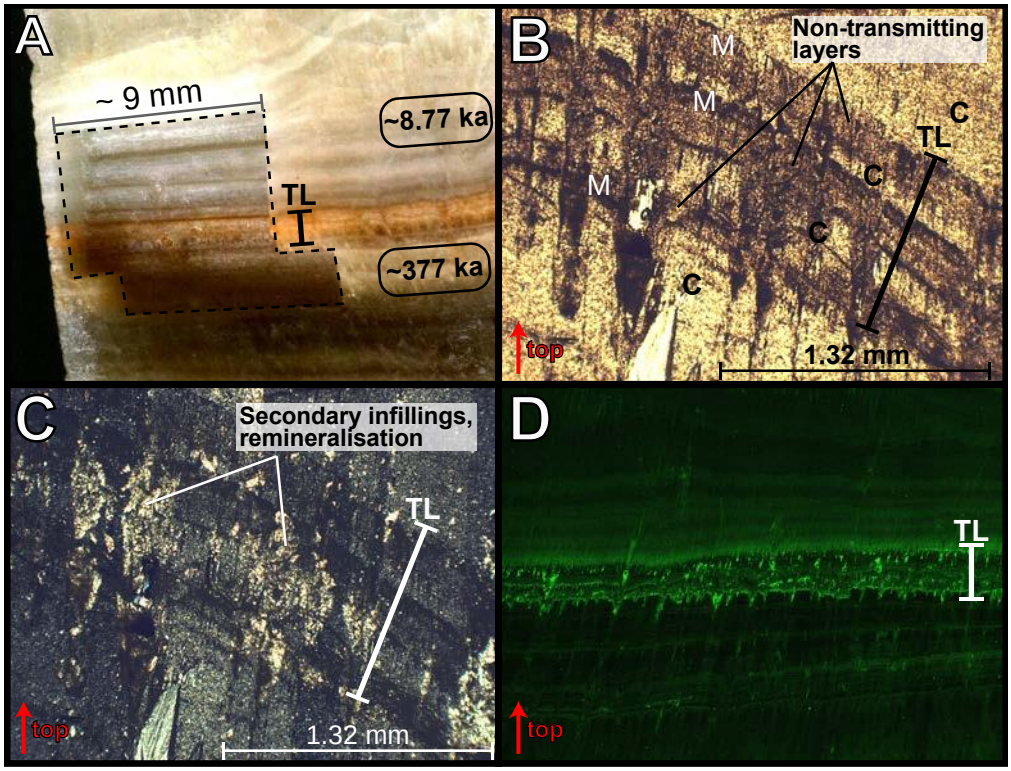

Fig. 3: Sampling and petrography of stalagmite SOP-20: A – High-resolution image of the sampled interval of the stalagmite, with the sampling trench highlighted by the dashed line. Ages (in boxes) refer to previous high-precision U-Th ages (Vaks et al., 2013) and their depth relative to the sampling trench. The black line, labelled TL, shows what we define as the transition layer and is also shown in B, C, and D. B, C – Thin section photographs of the transition layer at 4x magnification. B is under plane polarised light, C under cross polarised light. Relevant petrographic features are indicated on the scan (C – columnar calcite, M – micrite). D – Confocal fluorescence image of the transition layer using combined 405 and 488 nm excitation wavelengths (4x magnification).

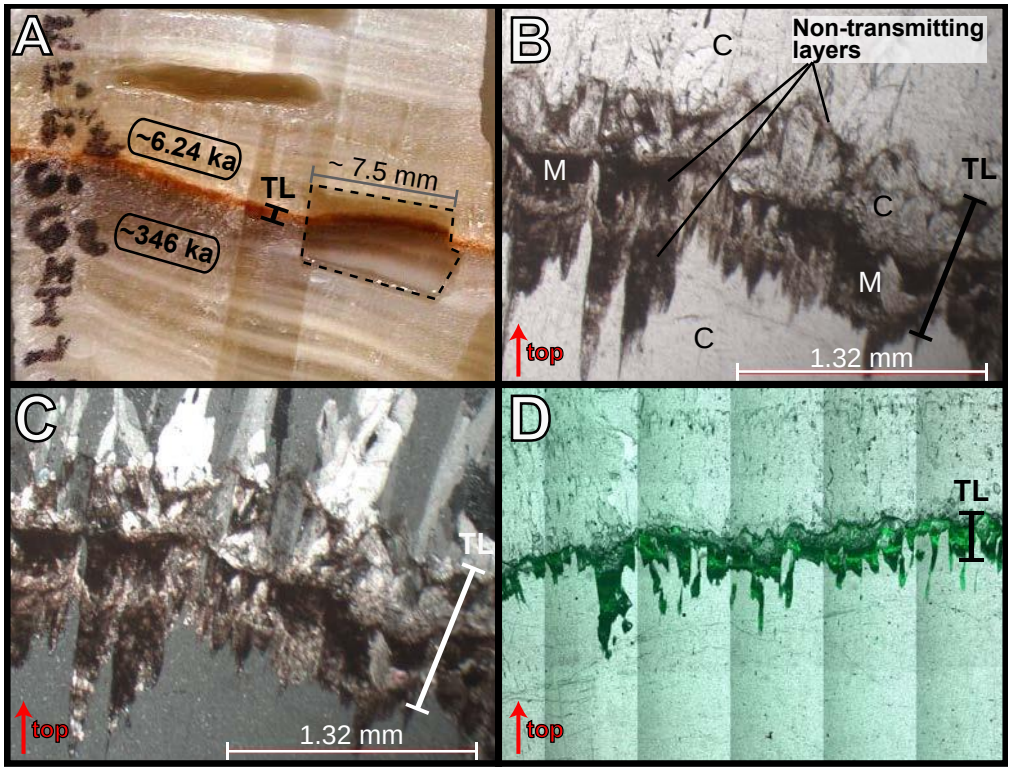

Fig. 4: Sampling and petrography of stalagmite SOP-18: A – High-resolution image of the sampled interval of the stalagmite, with the sampling trench highlighted by the dashed line. Ages (in boxes) refer to previous high-precision U-Th ages (Vaks et al., 2013) and their depth relative to the sampling trench. TL: transition layer, also in B, C, and D). B, C – Thin section photographs of the transition layer at 4x magnification. B is under plane polarised light, C under cross polarised light. Relevant petrographic features are indicated on the scan (C – columnar calcite, M – micrite). D – Confocal fluorescence image of the transition layer using combined 405 and 488 nm excitation wavelengths (4x magnification).

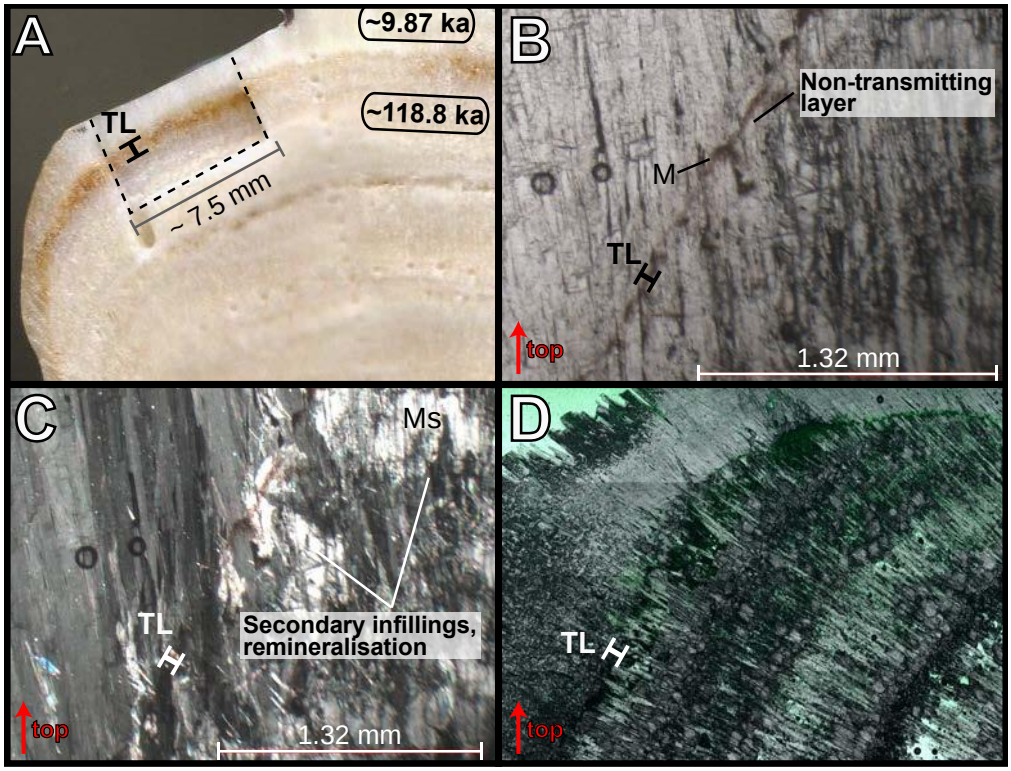

342

343 Fig 5: Sampling and petrography of stalagmite SB-pk7497: A – High-resolution image
344 of the sampled interval of the stalagmite, with the sampling trench highlighted by the
345 dashed line. Ages (in boxes) refer to previous high-precision U-Th ages (Vaks et al.,
346 2013) and their depth relative to the sampling trench. TL: transition layer, also in B, C,
347 and D). B, C – Thin section photographs of the transition layer at 4x magnification. B
348 is under plane polarised light, C under cross polarised light. Relevant petrographic
349 features are indicated on the scan (M – micrite, Ms – microsparite). D – Confocal
350 fluorescence image of the transition layer using combined 405 and 488 nm excitation
351 wavelengths (4x magnification).

352

353

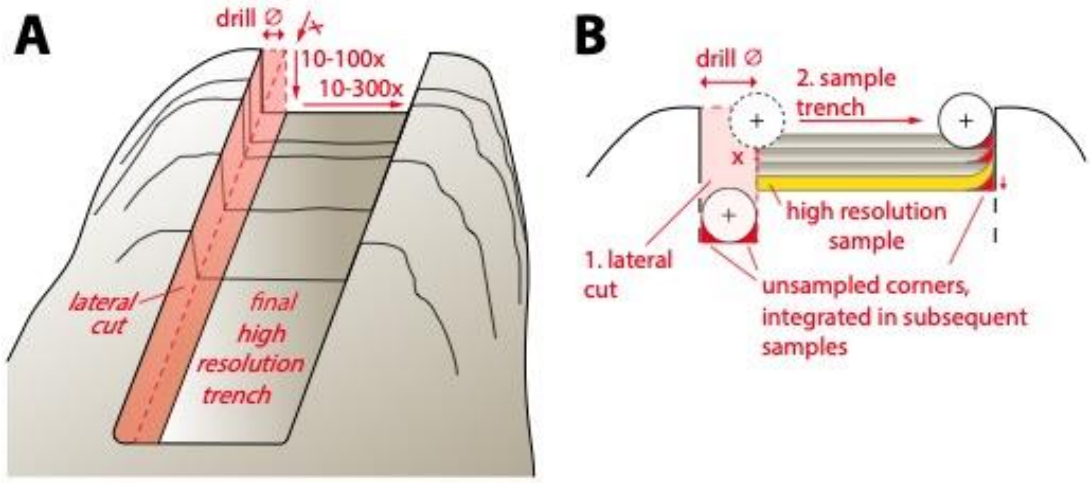

Fig 6: Schematic to indicate the high-resolution sampling strategy. A – View of the sampled stalagmite from top, B – Side view of the schematic sampling trench, identifying the high-resolution sample.

4.2. Stable isotopes and trace elements

No consistent changes in $\delta^{18}O$ values can be observed between the three stalagmites. SOP-20 and SB-pk7497 $\delta^{18}O$ values decrease between the two growth phases (Figs. 7 and 8B, Supplementary table 1), while in SOP-18, the $\delta^{18}O$ values slightly increase (Fig. 8A, Supplementary table 1).

All three stalagmites show an increase in $\delta^{13}C$ over the transition layer, but with differences in the amplitude of the change (Figs. 7 and 8, Supplementary table 1).

The concentrations of several trace elements strongly increase within the transition layers. In SOP-20, P, Mn, Cd, Ba, and U increase to several times the mean concentration observed in the rest of the sample (Fig. 7, Supplementary table 1). The enrichment in all these elements is expressed as a double peak in the transition layer. No significant enrichment is found for the elements Mg, Co, Cu, Sr, and Pb. The trends in trace elements are similar in SOP-18, but with only a single peak (Fig. 8A, Supplementary table 1). In this stalagmite, the enrichment over the transition layer is again very clear in P, Mn, Cd, Ba, and U, but additionally also in Cu and Pb. No significant enrichment is found for Mg, Co, and Sr. In stalagmite SB-pk7497 the enrichment in trace elements occurs at the beginning of the transition layer, rather than in the middle, as in SOP-20 and SOP-18 (Fig. 8B, Supplementary table 1). Here, only

Mn, Cu, Cd, and Pb show enrichment, while no trend can be distinguished for the other elements.

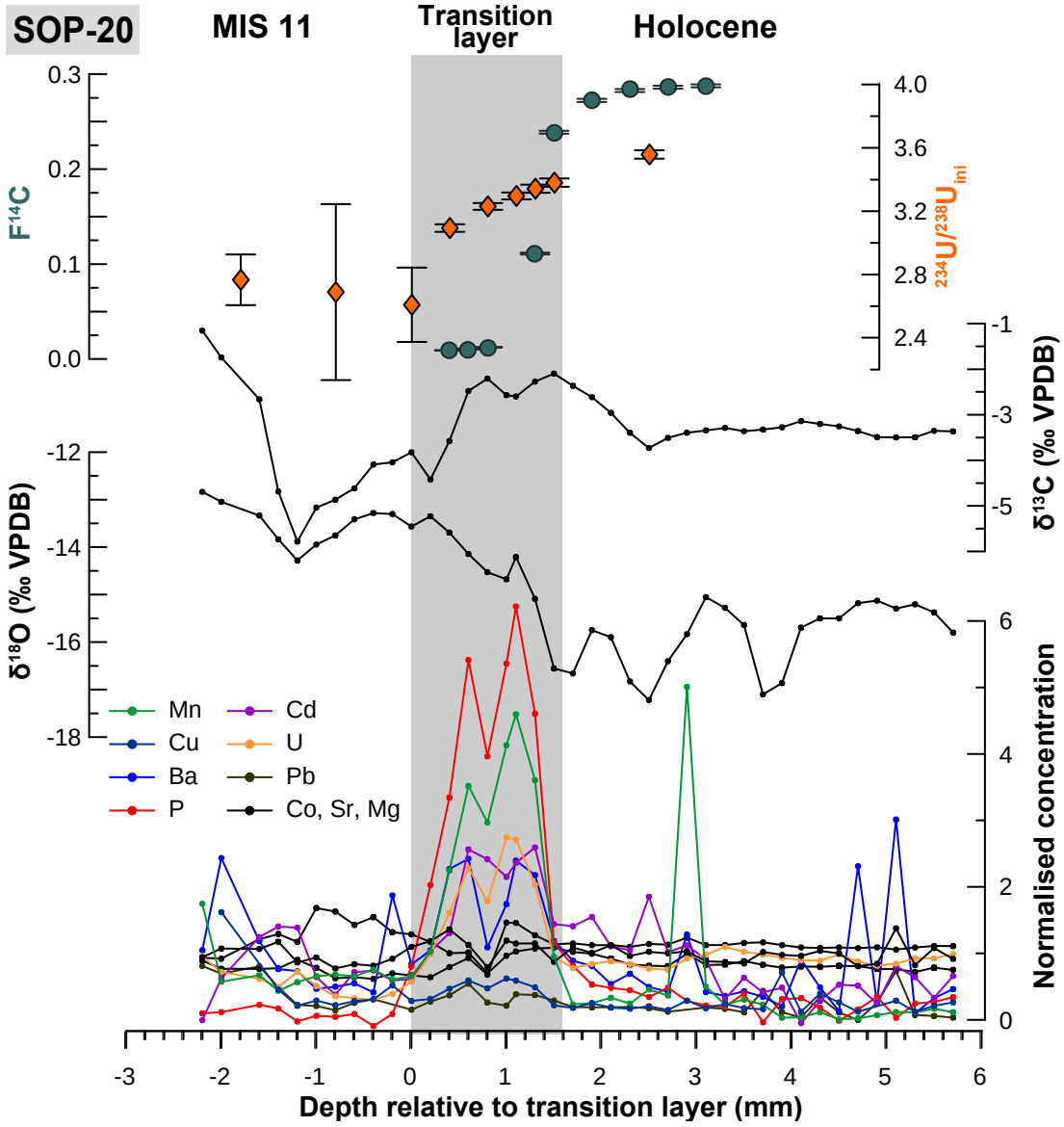

Fig 7: Results from geochemical analysis on stalagmite SOP-20. To ease intercomparison between the stalagmites, the measurement depth is normalised to the beginning of the transition layer (grey bar), defined as the start of increase in Mn concentrations. From top: $F^{14}C$, $^{234}U/^{238}U_{ini}$, $\delta^{13}C$, $\delta^{18}O$, and trace element concentrations (normalised against their average value).

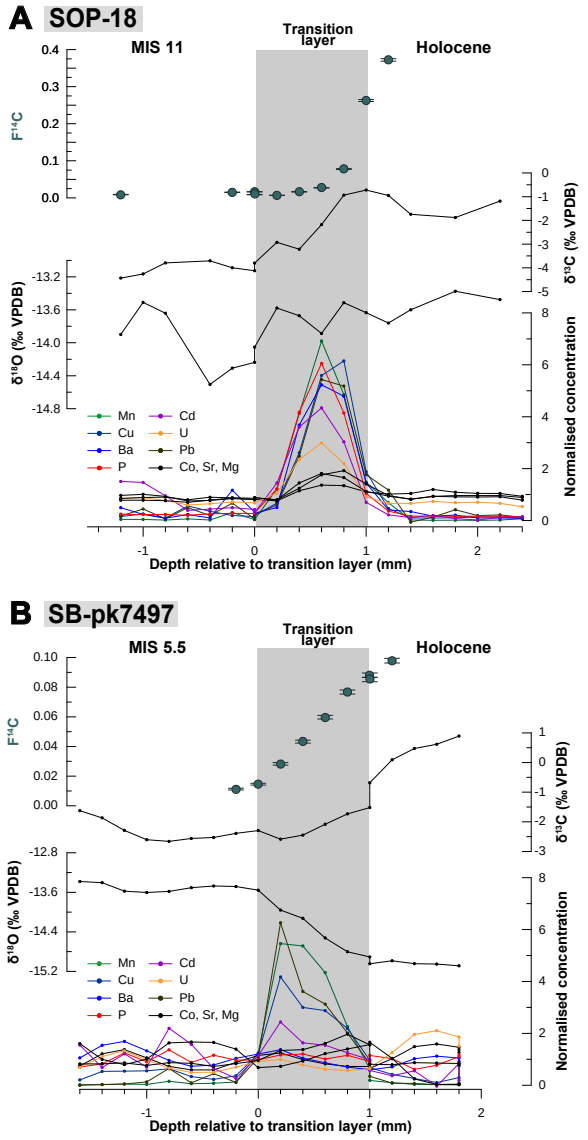

Fig 8: Results from geochemical analysis on stalagmites SOP-18 (A) and SB-pk7497 (B). To ease intercomparison between the stalagmites, the measurement depth is normalised to the beginning of the transition layer (grey bar), defined as the start of increase in Mn concentrations. For both stalagmites, from top: $F^{14}C$, $\delta^{13}C$, $\delta^{18}O$, and trace element concentrations (normalised against their average value).

4.3. U-Th dating of SOP-20

The high-resolution U-Th chronology of the transition layer in SOP-20 reveals an almost linear decrease in age from 400.0±36.3 (MIS 11) to 10.4±0.2 ka BP (early Holocene; Fig. 9A). Because of the high ^{238}U and low ^{232}Th content of the stalagmite (^{238}U: 0.47–5.3 ppm, ^{232}Th: 2.82–180.44 ppb) it was possible to achieve relatively high precision results despite the small sample size used. Samples from the main growth phases are in agreement with the previous high-precision dating by Vaks et al. (2013)

(Figs. 9 and 10). U and Th concentrations show a clear peak within the transition layer that matches the peak in the other trace elements (Fig. 10A and B). The ($^{232}Th/^{238}U$) ratio shows a maximum at the beginning of the transition layer, followed by a second smaller peak at the end of the layer, before transitioning towards the Holocene value (Fig. 10C). Initial ($^{234}U/^{238}U$) ratios (($^{234}U/^{238}U)_{ini}$), i.e. decay-corrected ($^{234}U/^{238}U$) values, are very high (2.61 – 3.56, Fig. 10D). A slight decrease in $(^{234}U/^{238}U)_{ini}$ before the transition layer is followed by a rapid increase within the layer. $(^{234}U/^{238}U)_{ini}$ ratios continue slightly to increase in the following Holocene growth phase.

4.4. Radiocarbon

In all three stalagmites, the studied interval covers the transition from a growth phase that is devoid of ^{14}C (either MIS 11 or MIS 5e depending on sample) to a growth phase within the ^{14}C range (early Holocene). Prior and at the beginning of the transition layer, $F^{14}C$ values are close to background levels ($F^{14}C$~0.01 for all stalagmites), but they are higher than the procedural blank milled from the base of SOP-20 ($F^{14}C$ = 0.002; Fig. 9B). In SOP-20 and SOP-18, $F^{14}C$ values only start to increase towards the end of the transition layer. In SB-pk7497, the general trend in $F^{14}C$ is very similar to SOP-20 and SOP-18, but $F^{14}C$ starts to increase directly at the beginning of the transition layer. The absolute $F^{14}C$ values in SB-pk7497 are much lower (early Holocene maximum: 0.097) than for the two stalagmites from Okhotnichya Cave, indicating a larger reservoir effect ('dead carbon fraction').

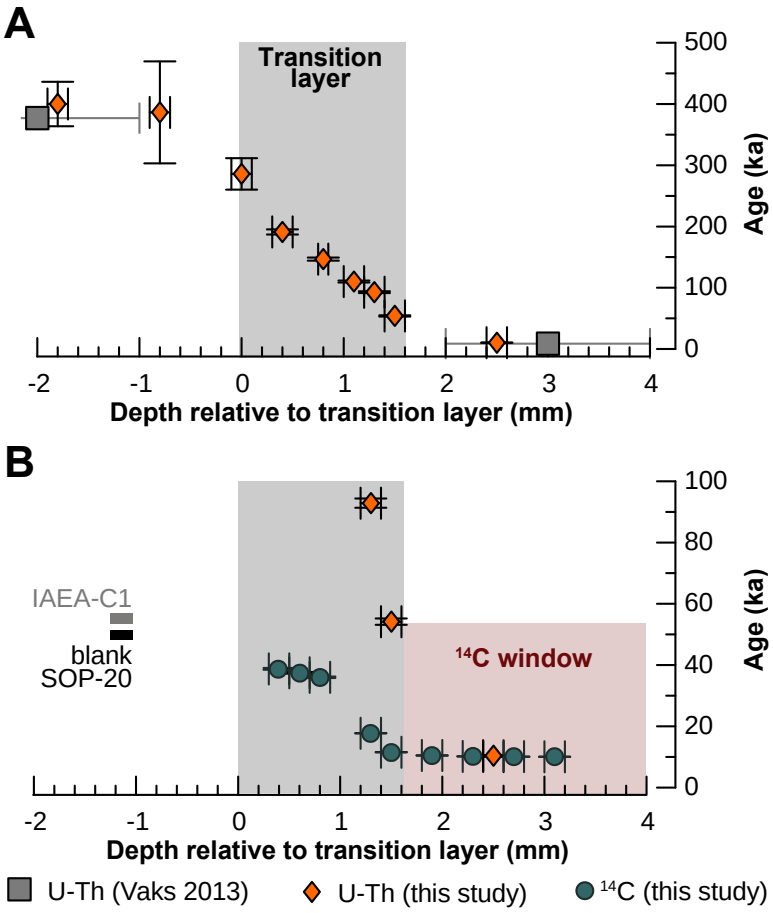

Fig 9: A – High-resolution U-Th chronology of the SOP-20 transition layer (this study, orange diamonds), compared to the previous high precision U-Th ages (grey squares) from Vaks et al. (2013). B – Comparison between high-resolution U-Th ages covering the last 100 ka and ^{14}C ages (green circles) in the transition layer. The ^{14}C age of the measured IAEA-C1 standard and the procedural stalagmite blank (milled from the base of SOP-20) are shown for comparison. The pink rectangle indicates where U-Th ages are younger than 55 ka, i.e., within the ^{14}C range. ^{14}C values above blank levels beyond this "window" have to be interpreted as resulting from sampling bias, i.e., mixing of older and younger material or from post-depositional infilling of porous spaces by younger material. Horizontal error bars denote uncertainty from sampling resolution.

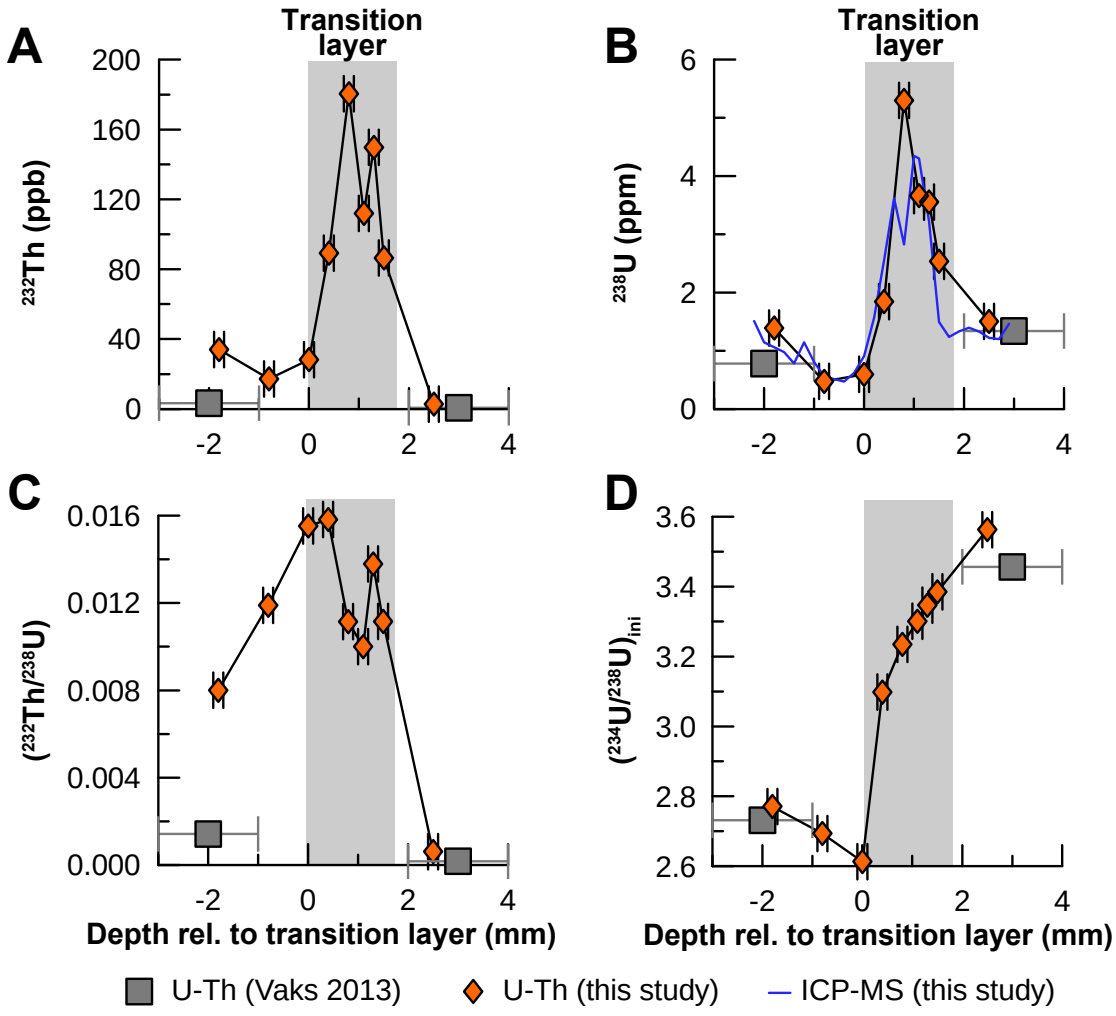

Fig 10: U and Th isotope measurements in stalagmite SOP-20. The transition layer is marked by the grey bar, and data is compared to the previous results from high-precision U-Th dating by Vaks et al. (2013; grey squares). Horizontal error bars denote uncertainty from sampling resolution. Isotope ratios are shown as activity ratios in round brackets.

5. Discussion

Permafrost degradation is often characterised by active-layer deepening and abrupt thermokarst formation, which can occur on the timescale of years (Schuur et al., 2015), thus requiring a highly sensitive archive that can capture high-frequency changes in surface biogeochemical cycling. The three stalagmites used in this study responded rapidly to climatic amelioration with the beginning of the Holocene by resuming their growth. Thus, it is possible that they also retained some information on permafrost thawing in the earliest carbonate deposited after the last glacial. The transition layers stand out as visibly anomalous intervals and reflect a change in the chemical

composition of the carbonate, which may be related to the overlaying permafrost deposit.

If the transition layers reflect anomalous early Holocene stalagmite growth related to increased carbon export from thawing permafrost deposits, we expect a diagnostic geochemical fingerprint in the carbonate. Increased organic matter concentrations would manifest in high levels of fluorescence, and in an enrichment in trace elements involved in the formation of organo-metal complexes in aqueous solutions (e.g., P, Mn, Cu, Zn, Pb, U; Borsato et al., 2007; Frisia et al., 2012; Hartland et al., 2012; Rutlidge et al., 2014). Low $\delta^{13}C$ values would be expected as a result of a higher proportion of biogenic carbon transported from the soil and epikarst by the drip water. Further, depleted ^{14}C values would signal the presence of high amounts of pre-aged organic matter stored in the permafrost.

However, alternative mechanisms could have led to the formation of the transition layers, including: i) chemical/diagenetic alteration (e.g., condensation-corrosion; Frisia, 2015; Martin-Pérez et al., 2012) of the stalagmite surface during periods of growth cessation; ii) anomalous growth at the end of the preceding growth phase; or, iii) episodic and/or very slow growth intervals throughout the period of "growth cessation". In the following, we will use the multi-proxy dataset from stalagmites SOP-20, SOP-18, and SB-pk7497 to discern which of these deposition mechanisms is the most likely scenario in the two caves studied here.

5.1. Age of the transition layer

The most straightforward method to define the timing of layer deposition is by dating them. The high-resolution U-Th chronology obtained from SOP-20 shows no prolonged hiatus between 400.0–10.4 ka BP, which suggests either very slow/episodic growth throughout most of the interval, or the presence of an artefact stemming from mixing of two carbonate end-members with very different U and Th isotopic compositions, i.e., a sampling bias. Because of the irregular surface of the transition layer in SOP-20 (Fig. 3) and the physical constraints from sampling (milling trench depth and width), it is very likely that some mixing between old (MIS 11) and young (Holocene) carbonate occurred.

The importance of mixing can be evaluated through a two end-member mass-balance using both the U-Th and ^{14}C data (see supplementary material for details). The ^{14}C

content in SOP-20 starts to increase in the last two samples within the transition layer (Supplementary table 1), and can be used to explore the mixing hypothesis. These samples have appreciable ^{14}C content, while U-Th ages suggest significantly older ages than straightforward ^{14}C ages. Using the ^{14}C and U-Th compositions of samples above and below these two samples as mixing end-members, the fractions of fossil and Holocene carbon required to give the ^{14}C and U-Th composition of the two samples can be calculated (see supplementary material for details). The consistency between results for ^{14}C, and those for the U-Th system, which have very different half-lives, then provides an assessment of the likelihood that mixing can explain the observations. We find that ^{14}C and U-Th ages for the two samples nearest the top of the transition layer can reasonably be explained by mixing of sample material from above and below, indicating that mixing on a length scale of tenths of millimetres has probably occurred during sampling of the transition layer. Because of this, these ages cannot be used as reliable markers for growth resumption, and this prevents us from being able to further resolve the timing of permafrost degradation at this location.

While mixing is probably responsible for the linear decrease in age of the last two samples in the transition layer (Fig. 9B), we suggest that the long-term decrease in U-Th ages over the entire layer is real. This is because the peaks in ^{238}U, ^{232}Th, and trace element concentrations within the transition layer (Figs. 7, 10A and B) cannot be explained with a two end member mixing scenario (Supplementary figure 1). Consequently, the high-resolution U-Th chronology obtained for the transition layer in SOP-20 clearly shows that the layer did not grow during the early Holocene. Instead, the regular decrease in age suggests that very slow or episodic growth between MIS 11 and the early Holocene occurred.

Mixing between fossil and Holocene carbon sources could also be responsible for the slightly elevated $F^{14}C$ values at the beginning of the transition layer in SOP-20 (Fig. 9B), as only a very small amount of modern carbon (4-5%) would be needed to explain these values. However, these samples coincide with the peak in trace elements, ^{238}U, and ^{232}Th (Figs. 7 and 10B), where mixing is expected to play a minor role. Subsequent infilling of porous spaces with carbon of early Holocene age after growth resumption is another possible mechanism that could lead to the observed elevated $F^{14}C$ values, without affecting the other, in this case less sensitive, geochemical parameters.

For SOP-18 and SB-pk7497, where no high-resolution U-Th chronology exists, it is more difficult to determine the timing of carbonate deposition and the role of mixing. In SOP-18 the patterns in trace element concentrations and $F^{14}C$ are very similar to SOP-20. Combined with the similarities in the crystal fabrics of the transition layer this suggests that the formation process of the transition layer in this stalagmite is likely the same as for SOP-20. In SB-pk7497, on the other hand, the rise in $F^{14}C$ values and the peak in trace elements occur at the beginning of the transition layer, suggesting that mixing might play a more important role here. Given that the transition layer in SB-pk7497 also displays strong signs of post-depositional alteration, we refrain from further interpreting the geochemical signatures in this sample.

5.2. Textural and elemental evidence for the formation mechanism of the transition

The transition layers in SOP-20 and SOP-18 are composed of 2-3 dark, non-light-transmitting and strongly fluorescing layers, intercalated with thin bands of clear calcite (Figs. 3 and 4). Dark and non-light-transmitting material with no clear crystal structure visible under the microscope can be micritic calcite (crystals $\leq$2 μm) or organic material, or a combination of both (Frisia, 2015). The presence of micrite in speleothems is poorly understood, as its formation requires high supersaturation and/or availability of large numbers of crystallisation nuclei, or the presence of organic compounds, and is often bio-mediated (Frisia, 2015; Morse et al., 2003). "Stromatolite-like" micrite fabrics suggesting the presence of microbial mats on the stalagmite surface (Frisia et al., 2012) have been described in stalagmites from a range of different environments, e.g., northern Italy (Frisia and Borsato, 2010), the Nullarbor Plain of southern Australia (Frisia et al., 2012), and a sub-glacier cave in the Swiss Alps (Luetscher et al., 2011). High fluorescence, indicating elevated concentrations of organic compounds, is typically observed in conjunction with micrite fabric, and corroborates the interpretation of microbial processes influencing their formation (Frisia, 2015). Microscopy shows that the dark material replaces dissolved columnar fabrics at the end of the preceding growth phase, possibly indicating *in-situ* production by cave-dwelling microbial mats, rather than transport into the cave from the epikarst and host rock (Frisia et al., 2012). Apart from localised neomorphism there is no evidence for extensive textural changes in SOP-20 and SOP-18, e.g., mosaic or

554 microsparite fabrics resulting from diagenetic alteration of the entire layer (Bajo et al.,
555 2016; Frisia, 2015; Scholz et al., 2014). In stalagmite SB-pk7497, however, the primary
556 aragonite has been replaced by mosaic calcite fabrics just before the transition,
557 suggesting a more prominent role of alteration in the formation of this diagenetic layer.
558
559 Several trace elements (P, Mn, Cu, Cd, Ba, Pb, U) are strongly enriched in the transition
560 layers of the stalagmites. The transport of elements such as P, Co, Cu, Pb, and U in
561 aqueous solutions with pH values typical of cave environments (~8) is dominated by
562 complexation with organic ligands, both in the colloidal and dissolved fractions
563 (Hartland et al., 2012; Hartland and Zitoun, 2018). These elements could therefore
564 serve as proxies for surface biological productivity and local karst hydrology (Borsato
565 et al., 2007; Hartland and Zitoun, 2018; Regattieri et al., 2016; Rutlidge et al., 2014),
566 and might be particularly sensitive chemical tracers for the mobilisation of permafrost
567 carbon (Pokrovsky et al., 2011). Speleothem P in particular is often invoked as a
568 palaeoproductivity and palaeohydrology proxy (Borsato et al., 2007; Huang et al.,
569 2001; Regattieri et al., 2016; Treble et al., 2003), as P is thought to be sourced from the
570 decay of vegetation, and transported to the cave as soluble hydrolysed phosphate or
571 complexed with organic colloids during periods of high water flux. However, other
572 studies have highlighted the occurrence of elevated P concentrations in conjunction
573 with petrographic features that suggest the presence of microbial mats (i.e.,
574 “stromatolite-like” laminae; Frisia et al., 2012; Jones, 2009). Similarly, Mn deposits in
575 caves have often been interpreted as the product of microbial participation (Barton and
576 Northup, 2007; Gázquez et al., 2011; Northup et al., 2003). Mn-rich layers have
577 previously been described in a stalactite from Botovskaya Cave, where they were
578 interpreted as formed by microbial processes during periods of warm climate, when the
579 absence of permafrost and enhanced soil weathering and erosion resulted in a higher
580 Mn flux to the cave (Pacton et al., 2013). However, the layers found by Pacton et al.
581 (2013) were asymmetrically distributed on one side of the stalactite and intercalated
582 with calcite, and thus are very different from the transition layers found in our study,
583 where the Mn-rich phases are clearly separated from the main growth phases.
584
585 Other formation mechanisms for the transition layers are difficult to reconcile with their
586 morphology, fluorescent properties, elemental composition, and age. For example,
587 condensation-corrosion processes through temperature differentials (e.g., from cave

588 ventilation) can lead to the alteration of speleothem carbonate and the formation of
589 micrite-like layers (Martín-Pérez et al., 2012; Palmer and Palmer, 2012). These
590 condensation-corrosion processes, however, cannot adequately explain the
591 fluorescence and elemental composition of the transition layers in SOP-20 and SOP-
592 18. Moreover, near-freezing temperatures in (sub-)arctic caves limit the transport
593 distance of moisture, and condensation is only expected near the entrances (Lauriol et
594 al., 2006) so is unlikely to occur in the deeper passages from where the stalagmites of
595 this study were collected. Ice deposition, in particular near the entrances, is documented
596 for Okhotnichya Cave (Bazarova et al., 2014) and Botovskaya Cave. Another potential
597 mechanism that could lead to increased concentrations of trace elements and organic
598 matter in karst seepage water is through partial freezing of groundwater during transport
599 in the subsurface. This cryochemical process leading to increased element and
600 dissolved organic matter content of the water is well described in polar rivers and lakes
601 where seasonal freeze-thawing cycles occur (Borysiak et al., 2015; Healy et al., 2006;
602 Mazurek et al., 2012; Schmidt et al., 1991; Xue et al., 2015). However, such a process
603 would likely lead to increases in all trace elemental concentrations, which is not what
604 we observe in the transition layers (Figs. 7 and 8). It is likely that differences in how
605 elements are dominantly incorporated in speleothem carbonate, i.e., substitution for Ca
606 in the crystal lattice (Mg, Sr, Ba), or within the colloidal fraction (e.g., P, Mn; Fairchild
607 and Treble, 2009), play a role in their concentration in the transition layer, as increased
608 concentrations of the former would require carbonate precipitation upstream of the cave
609 ('prior calcite/aragonite precipitation'). At present, we can therefore not exclude this
610 process to have some influence on the geochemistry of the transition layers in SOP-20
611 and SOP-18. However, their petrography suggests an important contribution from
612 microbial processes, and thus it is likely that the enrichment in P, Mn, and other trace
613 elements reflects *in-situ* biological productivity from microbial mats, rather than a
614 surface signal of vegetation productivity, permafrost stability, or cryochemical
615 processes. While we cannot at this stage definitively link the formation of the transition
616 layers in SOP-20 and SOP-18 to microbial mediation, the combined evidence from
617 petrography and geochemistry is compelling.
618
619 **5.3. History of growth of the transition layer**
620 Petrographic and geochemical (e.g., chronological) evidence suggests that episodic,
621 and likely very slow growth occurred in stalagmites SOP-20 (and possibly SOP-18)

between ~400 and ~10 ka BP (Fig. 9A). Although our dataset is not sufficiently highly resolved to unequivocally attribute a time frame to these growth episodes, it is probable that they represent interglacials between MIS 11 and the Holocene (i.e., MIS 9, 7, and 5e). Stalagmite growth did occur in Okhotnichya Cave during all interglacials of the past 500 ka, but MIS 11 appears to have been a particularly warm and prolonged interglacial in this region, causing widespread permafrost thaw up to 60°N (Vaks et al., 2013). Evidence for unusual warmth in Siberia during MIS 11 is additionally provided by high biogenic silica fractions in the sediments of Lake Baikal (Prokopenko et al., 2001) and high spruce content in Lake El'gygytgyn (Melles et al., 2012), which suggest regional temperatures 4-5°C above present.

With incipient glacial conditions at the end of MIS 11, water percolation into the cave stopped, allowing microbial mats to grow on the surface of the stalagmites, partially corroding/dissolving the underlying stalagmite surface. When surface conditions improved during a subsequent warm phase, this might have allowed for some water percolation through the epikarst, leading to a brief period of inorganic speleothem growth, followed again by microbial colonisation when climate deteriorated. Finally, widespread permafrost degradation occurred with the beginning of the Holocene, and inorganic growth resumed as the main growth mechanism. It is likely that highly localised factors are responsible for the absence of growth during MIS 9 and 5e in SOP-20 and SOP-18, primarily the location of the stalagmites in the cave in relation to the surface and percolation pathways through degrading permafrost, but possibly also non-climatic factors such as local tectonics. Permafrost and snow cover would be more persistent above caves with northward ground surface exposure, or located in depressions (e.g., dolines). Permafrost thaw is also unlikely to follow a single front, but would be modulated by the fracture network in the host rock (Žák et al., 2012), so that some drip sites might become active while others still remained frozen. Such conditions could have prevented speleothem growth from starting during MIS 9-5e, but it is possible that particularly warm periods during these interglacials could have led to episodic partial degradation of permafrost, and brief periods of inorganic speleothem growth. Cryogenic cave carbonate deposits may be able to resolve such brief and partial periods of thaw in more detail, as their formation typically precedes speleothem formation (Bazarova et al., 2014; Luetscher et al., 2013; Žák et al., 2012). Moreover, techniques employing ultra high-resolution measurements, e.g., nanoSIMS, synchrotron radiation, elemental mapping, or µXRF might be more successful at

extracting very high frequency variations that allow more detailed insight into processes during these "skipped" interglacials, but would be difficult to interpret without additional chronological control. Finally, it is possible that the delayed response of deep permafrost containing little carbon played a role in filtering out a surface geochemical signal of degrading permafrost in the stalagmites.

6. Conclusions

This study investigated the potential of stalagmites as precisely dated, high-resolution, and highly localised archives to record processes occurring during permafrost thawing. We tested a suite of geochemical proxies, supported by U-Th dating and petrographic analyses, on three stalagmites from Okhotnichya and Botovskaya caves in Siberia. We find that the transition layers between subsequent interglacial growth phases are characterised by complex petrography and geochemistry, and possibly reflect very slow or episodic growth phases during glacials or "skipped" interglacials, interrupted by the development of microbial mats during periods when abiotic growth stops. This allows us to considerably refine our understanding of stalagmite growth processes and forcings in these caves.

Evidence for a geochemical record of permafrost degradation, on the other hand, remains elusive. This might be related to low sensitivity of the archive in capturing the chemical signatures of surface processes, especially considering the often very rapid timescale of permafrost degradation and the typically slow growth rates of stalagmites in caves at near-freezing conditions. We conclude that it is generally unlikely that stalagmites will be able to provide more detailed answers to processes related to permafrost degradation.

Acknowledgements:

We thank Philip Holdship and Chris Day at the Department of Earth Sciences, University of Oxford, for their help with the ICP-MS and stable isotope measurements. David Chivall and Prof. Tom Higham are gratefully acknowledged for their help and expertise with the radiocarbon analysis at the Oxford Radiocarbon Unit. We thank Owen Green and Jonathan Wells (Department of Earth Sciences, University of Oxford) for preparation of thin sections and microscopy assistance. Prof. Tim Eglinton at the Department of Earth Sciences, ETH Zurich, and the staff at the Laboratory for Ion Beam Physics (LIP) at ETH Zurich are thanked for their support in the gas ion source

690 ^{14}C measurements. Andrew Jefferson and Micron Oxford (Department of
691 Biochemistry, University of Oxford) are gratefully acknowledged for access to
692 microscopes and help with the fluorescence analysis of the thin sections. Marcelo
693 Rosensaft and Alex Borshevsky from Geological Survey of Israel are thanked for
694 generating the map used in Figure 1. We also thank our collaborating partners in Russia,
695 especially Alexander Kononov at the Department of Earth Crust of the Russian
696 Academy of Sciences in Irkutsk, and Alexander Osinzev and the Speleoclub Arabika
697 for their long-standing partnership with field expeditions and caving expertise. Two
698 anonymous reviewers and the editorial team at Quaternary Geochronology are thanked
699 for their critical assessment and feedback, which greatly improved the manuscript.
700 F.A.L. gratefully acknowledges funding of this research by the Swiss National Science
701 Foundation Early postdoc mobility scheme (grant number: P2EZP2_172213).
702
703 **References**
704 Atkinson, T.C., Harmon, R.S., Smart, P.L., Waltham, A.C., 1978. Palaeoclimatic and
705 geomorphic implications of $^{230}Th/^{234}U$ dates on speleothems from Britain.
706 Nature 272, 24–28.
707 Bajo, P., Borsato, A., Drysdale, R., Hua, Q., Frisia, S., Zanchetta, G., Hellstrom, J.,
708 Woodhead, J., 2017. Stalagmite carbon isotopes and dead carbon proportion
709 (DCP) in a near-closed-system situation: An interplay between sulphuric and
710 carbonic acid dissolution. Geochim. Cosmochim. Acta 210, 208–227.
711 doi:10.1016/j.gca.2017.04.038
712 Bajo, P., Hellstrom, J., Frisia, S., Drysdale, R., Black, J., Woodhead, J., Borsato, A.,
713 Zanchetta, G., Wallace, M.W., Regattieri, E., Haese, R., 2016. "Cryptic"
714 diagenesis and its implications for speleothem geochronologies. Quat. Sci. Rev.
715 148, 17–28. doi:10.1016/j.quascirev.2016.06.020
716 Barton, H.A., Northup, D.E., 2007. Geomicrobiology in cave environments: past,
717 current and future perspectives. J. Cave Karst Stud. 69, 163–178.
718 Bazarova, E.P., Kononov, A.M., Gutareva, O.S., Nartova, N. V., 2014. Specific
719 characteristics of cryogenic mineral formations of Okhotnichya cave in Pre-
720 Baikal area (Irkutsk region). Earth's Cryosph. 18, 62–71.
721 Bergel, S.J., Carlson, P.E., Larson, T.E., Wood, C.T., Johnson, K.R., Banner, J.L.,
722 Breecker, D.O., 2017. Constraining the subsoil carbon source to cave-air CO_2
723 and speleothem calcite in central Texas. Geochim. Cosmochim. Acta 217, 112–

127. doi:10.1016/j.gca.2017.08.017
Biskaborn, B.K., Smith, S.L., Noetzli, J., Matthes, H., Vieira, G., Streletskiy, D.A., Schoeneich, P., Romanovsky, V.E., Lewkowicz, A.G., Abramov, A., Allard, M., Boike, J., Cable, W.L., Christiansen, H.H., Delaloye, R., Diekmann, B., Drozdov, D., Etzelmüller, B., Grosse, G., Guglielmin, M., Ingeman-Nielsen, T., Isaksen, K., Ishikawa, M., Johansoon, M., Johannson, H., Joo, A., Kaverin, D., Kholodov, A., Konstantinov, P., Kröger, T., Lambiel, C., Lanckman, J.-P., Luo, D., Malkova, G., Meiklejohn, J., Moskalenko, N., Oliva, M., Phillips, M., Ramos, M., Sannel, A.B.K., Sergeev, D., Seybold, C., Skryabin, P., Vasiliev, A., Wu, Q., Yoshikawa, K., Zhelenznyak, M., Lantuit, H., 2019. Permafrost is warming at a global scale. Nat. Commun. 10. doi:10.1038/s41467-018-08240-4
Borsato, A., Frisia, S., Fairchild, I.J., Somogyi, A., Susini, J., 2007. Trace element distribution in annual stalagmite laminae mapped by micrometer-resolution X-ray fluorescence: Implications for incorporation of environmentally significant species. Geochim. Cosmochim. Acta 71, 1494–1512. doi:10.1016/j.gca.2006.12.016
Borysiak, J., Grześ, M., Pulina, M., Szpikowska, G., 2015. Hydrogeochemical and biogeochemical processes in Kaffiøyra river catchments (Spitsbergen, Norway). Quaest. Geogr. 34, 111–124. doi:10.1515/quageo-2015-0010
Brock, F., Higham, T., Ditchfield, P., Bronk Ramsey, C., 2010. Current Pretreatment Methods for AMS Radiocarbon Dating at the Oxford Radiocarbon Accelerator Unit (ORAU). Radiocarbon 52, 103–112. doi:10.1017/S0033822200045069
Columbu, A., Drysdale, R., Hellstrom, J., Woodhead, J., Cheng, H., Hua, Q., Zhao, J., Montagna, P., Pons-Branchu, E., Edwards, R.L., 2019. U-Th and radiocarbon dating of calcite speleothems from gypsum caves (Emilia Romagna, North Italy). Quat. Geochronol. 52, 51–62. doi:10.1016/j.quageo.2019.04.002
Comyn-Platt, E., Hayman, G., Huntingford, C., Chadburn, S.E., Burke, E.J., Harper, A.B., Collins, W.J., Webber, C.P., Powell, T., Cox, P.M., Gedney, N., Sitch, S., 2018a. Carbon budgets for 1.5 and 2°C targets lowered by natural wetland and permafrost feedbacks. Nat. Geosci. 11, 568–573.
Comyn-Platt, E., Hayman, G., Huntingford, C., Chadburn, S.E., Burke, E.J., Harper, A.B., Collins, W.J., Webber, C.P., Powell, T., Cox, P.M., Gedney, N., Sitch, S., 2018b. Author correction: Carbon budgets for 1.5 and 2 °C targets lowered by natural wetland and permafrost feedbacks. Nat. Geosci. 11, 882–886.

758 doi:10.1038/s41561-018-0174-9
759 Day, C.C., Henderson, G.M., 2011. Oxygen isotopes in calcite grown under cave-
760 analogue conditions. Geochim. Cosmochim. Acta 75, 3956–3972.
761 doi:10.1016/j.gca.2011.04.026
762 Fahrni, S.M., Wacker, L., Synal, H.-A., Szidat, S., 2013. Improving a gas ion source
763 for ^{14}C AMS. Nucl. Instruments Methods Phys. Res. B 294, 320–327.
764 doi:10.1016/j.nimb.2012.03.037
765 Fairchild, I.J., Treble, P.C., 2009. Trace elements in speleothems as recorders of
766 environmental change. Quat. Sci. Rev. 28, 449–468.
767 doi:10.1016/j.quascirev.2008.11.007
768 Filippov, A.G., 2000. Speleogenesis of Botovskaya Cave, Eastern Siberia, Russia, in:
769 Speleogenesis: Evolution of Karst Aquifers. National Speleological Society,
770 Huntsville, pp. 282–286.
771 Frisia, S., 2015. Microstratigraphic logging of calcite fabrics in speleothems as tool
772 for palaeoclimate studies. Int. J. Speleol. 44, 1–16. doi:10.5038/1827-
773 806X.44.1.1
774 Frisia, S., Borsato, A., 2010. Karst, in: Developments in Sedimentology. pp. 269–318.
775 Frisia, S., Borsato, A., Drysdale, R.N., Paul, B., Greig, A., Cotte, M., 2012. A re-
776 evaluation of the palaeoclimatic significance of phosphorus variability in
777 speleothems revealed by high-resolution synchrotron micro XRF mapping. Clim.
778 Past 8, 2039–2051. doi:10.5194/cp-8-2039-2012
779 Gasser, T., Kechiar, M., Ciais, P., Burke, E.J., Kleinen, T., Zhu, D., Huang, Y., Ekici,
780 A., Obersteiner, M., 2019. Author correction: Path-dependent reductions in CO_2
781 emission budgets caused by permafrost carbon release. Nat. Geosci. 12, 80.
782 doi:10.1038/s41561-018-0273-7
783 Gasser, T., Kechiar, M., Ciais, P., Burke, E.J., Kleinen, T., Zhu, D., Huang, Y., Ekici,
784 A., Obersteiner, M., 2018. Path-dependent reductions in CO_2 emission budgets
785 caused by permafrost carbon release. Nat. Geosci. 11, 830–835.
786 doi:10.1038/s41561-018-0227-0
787 Gázquez, F., Calaforra, J.M., Forti, P., 2011. Black Mn-Fe crusts as markers of abrupt
788 palaeoenvironmental changes in El Soplao Cave (Cantabria, Spain). Int. J.
789 Speleol. 40, 163–169. doi:10.5038/1827-806X.40.2.8
790 Genty, D., Baker, A., Massault, M., Proctor, C., Gilmour, M., Pons-Branchu, E.,
791 Hamelin, B., 2001. Dead carbon in stalagmites: carbonate bedrock

792 paleodissolution vs. ageing of soil organic matter. Implications for ^{13}C variations
793 in speleothems. Geochim. Cosmochim. Acta 65, 3443–3457. doi:10.1016/S0016-
794 7037(01)00697-4
795 Griffiths, M.L., Fohlmeister, J., Drysdale, R.N., Hua, Q., Johnson, K.R., Hellstrom,
796 J.C., Gagan, M.K., Zhao, J. -x., 2012. Hydrological control of the dead carbon
797 fraction in a Holocene tropical speleothem. Quat. Geochronol. 14, 81–93.
798 doi:10.1016/j.quageo.2012.04.001
799 Grosse, G., Romanovsky, V.E., Jorgenson, T., Walter Anthony, K., Brown, J.,
800 Overduin, P.P., 2011. Vulnerability and feedbacks of permafrost to climate
801 change. Eos (Washington. DC). 92, 73–74. doi:10.1002/ppp.689
802 Hartland, A., Fairchild, I.J., Lead, J.R., Borsato, A., Baker, A., Frisia, S., Baalousha,
803 M., 2012. From soil to cave: transport of trace metals by natural organic matter
804 in karst dripwaters. Chem. Geol. 304–305, 68–82.
805 doi:10.1016/j.chemgeo.2012.01.032
806 Hartland, A., Zitoun, R., 2018. Transition metal availability to speleothems controlled
807 by organic binding ligands. Geochemical Perspect. Lett. 8, 22–25.
808 doi:10.7185/geochemlet.1824
809 Healy, M., Webster-Brown, J.G., Brown, K.L., Lane, V., 2006. Chemistry and
810 stratification of Antarctic meltwater ponds II: inland ponds in the McMurdo Dry
811 Valleys, Victoria Land. Antarct. Sci. 18, 525–533.
812 doi:10.1017/s0954102006000575
813 Hellstrom, J., 2006. U-Th dating of speleothems with high initial ^{230}Th using
814 stratigraphical constraint. Quat. Geochronol. 1, 289–295.
815 doi:10.1016/j.quageo.2007.01.004
816 Hjort, J., Karjalainen, O., Aalto, J., Westermann, S., Romanovsky, V.E., Nelson, F.E.,
817 Etzelmüller, B., Luoto, M., 2018. Degrading permafrost puts Arctic
818 infrastructure at risk by mid-century. Nat. Commun. 9. doi:10.1038/s41467-018-
819 07557-4
820 Huang, Y., Fairchild, I.J., Borsato, A., Frisia, S., Cassidy, N.J., McDermott, F.,
821 Hawkesworth, C.J., 2001. Seasonal variations in Sr, Mg and P in modern
822 speleothems (Grotta di Ernesto, Italy). Chem. Geol. 175, 429–448.
823 doi:10.1016/S0009-2541(00)00337-5
824 Hugelius, G., Strauss, J., Zubrzycki, S., Harden, J.W., Schuur, E.A.G., Ping, C.-L.,
825 Schirrmeister, L., Grosse, G., Michaelson, G.J., Koven, C.D., O'Donnell, J.A.,

826 Elberling, B., Mishra, U., Camill, P., Yu, Z., Palmtag, J., Kuhry, P., 2014.
827 Estimated stocks of circumpolar permafrost carbon with quantified uncertainty
828 ranges and identified data gaps. Biogeosciences 11, 6573–6593. doi:10.5194/bg-
829 11-6573-2014
830 Jones, B., 2011. Stalactite growth mediated by biofilms: example from Nani Cave,
831 Cayman Brac, British West Indies. J. Sediment. Res. 81, 322–338.
832 doi:10.2110/jsr.2011.28
833 Jones, B., 2009. Phosphatic precipitates associated with actinomycetes in speleothems
834 from Grand Cayman, British West Indies. Sediment. Geol. 219, 302–317.
835 doi:10.1016/j.sedgeo.2009.05.020
836 Jones, M.C., Yu, Z., 2010. Rapid deglacial and early Holocene expansion of peatlands
837 in Alaska. Proc. Natl. Acad. Sci. 107, 7347–7352. doi:10.1073/pnas.0911387107
838 Kuhry, P., Bárta, J., Blok, D., Elberling, B., Faucherre, S., Hugelius, G., Richter, A.,
839 Šantrůčková, H., Weiss, N., 2019. Lability classification of soil organic matter in
840 the northern permafrost region. Biogeosciences Discuss. doi:10.5194/bg-2019-89
841 Lauriol, B., Prévost, C., Lacelle, D., 2006. The distribution of diatom flora in ice
842 caves of the northern Yukon Territory, Canada: relationship to air circulation and
843 freezing. Int. J. Speleol. 35, 83–92. doi:10.5038/1827-806x.35.2.4
844 Luetscher, M., Borreguero, M., Moseley, G.E., Spötl, C., Edwards, R.L., 2013. Alpine
845 permafrost thawing during the Medieval Warm Period identified from cryogenic
846 cave carbonates. Cryosphere 7, 1073–1081. doi:10.5194/tc-7-1073-2013
847 Luetscher, M., Hoffmann, D.L., Frisia, S., Spötl, C., 2011. Holocene glacier history
848 from alpine speleothems, Milchbach cave, Switzerland. Earth Planet. Sci. Lett.
849 302, 95–106. doi:10.1016/j.epsl.2010.11.042
850 Martín-Pérez, A., Martín-García, R., Alonso-Zarza, A.M., 2012. Diagenesis of a
851 drapery speleothem from Castañar Cave: from dissolution to dolomitization. Int.
852 J. Speleol. 41, 251–266.
853 Mason, A.J., Henderson, G.M., 2010. Correction of multi-collector-ICP-MS
854 instrumental biases in high-precision uranium – thorium chronology. Int. J. Mass
855 Spectrom. 295, 26–35. doi:10.1016/j.ijms.2010.06.016
856 Mazurek, M., Paluszkiewicz, R., Rachlewicz, G., Zwoliński, Z., 2012. Variability of
857 water chemistry in tundra lakes, Petuniabukta coast, Central Spitsbergen,
858 Svalbard. Sci. World J. doi:10.1100/2012/596516
859 Melles, M., Brigham-Grette, J., Minyuk, P.S., Nowaczyk, N.R., Wennrich, V.,

DeConto, R.M., Anderson, P.M., Andreev, A.A., Coletti, A., Cook, T.L., Haltia-Hovi, E., Kukkonen, M., Lozhkin, A. V, Rosén, P., Tarasov, P., Vogel, H., Wagner, B., 2012. 2.8 Million years of arctic climate change from Lake El'gygytgyn, NE Russia. Science 337, 315–320.

Morse, J.W., Gledhill, D.K., Millero, F.J., 2003. $CaCO_3$ precipitation kinetics in waters from the Great Bahama Bank: Implications for the relationship between Bank hydrochemistry and whitings. Geochim. Cosmochim. Acta 67, 2819–2826. doi:10.1016/S0016-7037(03)00103-0

Mühlinghaus, C., Scholz, D., Mangini, A., 2007. Modelling stalagmite growth and $\delta^{13}C$ as a function of drip interval and temperature. Geochim. Cosmochim. Acta 71, 2780–2790. doi:10.1016/j.gca.2007.03.018

Northup, D.E., Barns, S.M., Yu, L.E., Spilde, M.N., Schelble, R.T., Dano, K.E., Crossey, L.J., Connolly, C.A., Boston, P.J., Natvig, D.O., Dahm, C.N., 2003. Diverse microbial communities inhabiting ferromanganese deposits in Lechuguilla and Spider Caves. Environ. Microbiol. 5, 1071–1086.

Pacton, M., Breitenbach, S.F.M., Lechleitner, F.A., Vaks, A., Rollion-Bard, C., Gutareva, O.S., Osintcev, A. V., Vasconcelos, C., 2013. The role of microorganisms in the formation of a stalactite in Botovskaya Cave, Siberia-paleoenvironmental implications. Biogeosciences 10, 6115–6130. doi:10.5194/bg-10-6115-2013

Palmer, M. V., Palmer, A.N., 2012. Petrographic and isotopic evidence for late-stage processes in sulfuric acid caves of the Guadalupe Mountains, New Mexico, USA. Int. J. Speleol. 41, 231–250.

Pokrovsky, O.S., Shirokova, L.S., Kirpotin, S.N., Audry, S., Viers, J., Dupré, B., 2011. Effect of permafrost thawing on organic carbon and trace element colloidal speciation in the thermokarst lakes of western Siberia. Biogeosciences 8, 565–583. doi:10.5194/bg-8-565-2011

Prokopenko, A.A., Krabanov, E.B., Williams, D.F., Kuzmin, M.I., Shackleton, N.J., Crowhurst, S.J., Peck, J.A., Gvozdkov, A.N., King, J.W., 2001. Biogenic silica record of the Lake Baikal response to climatic forcing during the Brunhes. Quat. Res. 55, 123–132. doi:10.1006/qres.2000.2212

Regattieri, E., Zanchetta, G., Drysdale, R.N., Isola, I., Woodhead, J.D., Hellstrom, J.C., Giaccio, B., Greig, A., Baneschi, I., Dotsika, E., 2016. Environmental variability between the penultimate deglaciation and the mid Eemian: Insights

from Tana che Urla (central Italy) speleothem trace element record. Quat. Sci. Rev. 152, 80–92. doi:10.1016/j.quascirev.2016.09.027

Reimer, P.J., Brown, T.A., Reimer, R.W., 2004. Discussion: reporting and calibration of post-bomb ^{14}C data. Radiocarbon 46, 1299–1304.

Richards, D.A., Dorale, J.A., 2003. Uranium-series chronology and environmental applications of speleothems. Rev. Mineral. Geochemistry 52, 407–460. doi:10.1515/9781501509308-015

Rutlidge, H., Baker, A., Marjo, C.E., Andersen, M.S., Graham, P.W., Cuthbert, M.O., Rau, G.C., Roshan, H., Markowska, M., Mariethoz, G., Jex, C.N., 2014. Dripwater organic matter and trace element geochemistry in a semi-arid karst environment: Implications for speleothem paleoclimatology. Geochim. Cosmochim. Acta 135, 217–230. doi:10.1016/j.gca.2014.03.036

Schmidt, S., Moskal, W., De Mora, S.J., Howard-Williams, C., Vincent, W.F., 1991. Limnological properties of Antarctic ponds during winter freezing. Antarct. Sci. 3, 379–388. doi:10.1017/s0954102091000482

Scholz, D., Tolzmann, J., Hoffmann, D.L., Jochum, K.P., Spötl, C., Riechelmann, D.F.C., 2014. Diagenesis of speleothems and its effect on the accuracy of $^{230}Th/U$-ages. Chem. Geol. 387, 74–86. doi:10.1016/j.chemgeo.2014.08.005

Schuur, E.A.G., McGuire, A.D., Schädel, C., Grosse, G., Harden, J.W., Hayes, D.J., Hugelius, G., Koven, C.D., Kuhry, P., Lawrence, D.M., Natali, S.M., Olefeldt, D., Romanovsky, V.E., Schaefer, K., Turetsky, M.R., Treat, C.C., Vonk, J.E., 2015. Climate change and the permafrost carbon feedback. Nature 520, 171–179. doi:10.1038/nature14338

Synal, H.A., Stocker, M., Suter, M., 2007. MICADAS: A new compact radiocarbon AMS system. Nucl. Instruments Methods Phys. Res. B 259, 7–13. doi:10.1016/j.nimb.2007.01.138

Tesi, T., Muschitiello, F., Smittenberg, R.H., Jakobsson, M., Vonk, J.E., Hill, P., Andersson, A., Kirchner, N., Noormets, R., Dudarev, O., Semiletov, I., Gustafsson, Ö., 2016. Massive remobilization of permafrost carbon during post-glacial warming. Nat. Commun. 7. doi:10.1038/ncomms13653

Tisato, N., Torriani, S.F.F., Monteux, S., Sauro, F., De Waele, J., Tavagna, M.L., D'Angeli, I.M., Chailloux, D., Renda, M., Eglinton, T.I., Bontognali, T.R.R., 2015. Microbial mediation of complex subterranean mineral structures. Sci. Rep. 5. doi:10.1038/srep15525

928 Treble, P., Shelley, J.M.G., Chappell, J., 2003. Comparison of high resolution sub-
929 annual records of trace elements in a modern (1911-1992) speleothem with
930 instrumental climate data from southwest Australia. Earth Planet. Sci. Lett. 216,
931 141–153. doi:10.1016/S0012-821X(03)00504-1
932 Vaks, A., Gutareva, O.S., Breitenbach, S.F.M., Avirmed, E., Mason, A.J., Thomas,
933 A.L., Osinzev, A. V, Kononov, A.M., Henderson, G.M., 2013. Speleothems
934 Reveal 500,000-Year History of Siberian Permafrost. Science 340, 183–186.
935 doi:10.1126/science.1228729
936 van Beynen, P., Bourbonniere, R., Ford, D., Schwarcz, H., 2001. Causes of colour
937 and fluorescence in speleothems. Chem. Geol. 175, 319–341.
938 doi:10.1016/S0009-2541(00)00343-0
939 van Calsteren, P., Thomas, L., 2006. Uranium-series dating applications in natural
940 environmental science. Earth-Science Rev. 75, 155–175.
941 doi:10.1016/j.earscirev.2005.09.001
942 Walter Anthony, K., Schneider von Deimling, T., Nitze, I., Frolking, S., Emond, A.,
943 Daanen, R., Anthony, P., Lindgren, P., Jones, B., Grosse, G., 2018. 21st-century
944 modeled permafrost carbon emissions accelerated by abrupt thaw beneath lakes.
945 Nat. Commun. 9. doi:10.1038/s41467-018-05738-9
946 Walter Anthony, K.M., Zimov, S.A., Grosse, G., Jones, M.C., Anthony, P.M., Chapin
947 III, F.S., Finlay, J.C., Mack, M.C., Davydov, S., Frenzel, P., Frolking, S., 2014.
948 A shift of thermokarst lakes from carbon sources to sinks during the Holocene
949 epoch. Nature 511, 452–456. doi:10.1038/nature13560
950 Wilcox, P.S., Dorale, J.A., Baichtal, J.F., Spötl, C., Fowell, S.J., Edwards, R.L.,
951 Kovarik, J.L., 2019. Millennial-scale glacial climate variability in Southeastern
952 Alaska follows Dansgaard-Oeschger cyclicity. Sci. Rep. 9. doi:10.1038/s41598-
953 019-44231-1
954 Williams, P.J., Warren, I.M.T., 1999. The English language edition of the
955 geocryological map of Russia and neighboring republics.
956 Winterfeld, M., Mollenhauer, G., Dummann, W., Köhler, P., Lembke-Jene, L.,
957 Meyer, V.D., Hefter, J., McIntyre, C., Wacker, L., Kokfelt, U., Tiedemann, R.,
958 2018. Deglacial mobilization of pre-aged terrestrial carbon from degrading
959 permafrost. Nat. Commun. 9. doi:10.1038/s41467-018-06080-w
960 Xue, S., Wen, Y., Hui, X., Zhang, L., Zhang, Z., Wang, J., Zhang, Y., 2015. The
961 migration and transformation of dissolved organic matter during the freezing

processes of water. J. Environ. Sci. (China) 27, 168–178. doi:10.1016/j.jes.2014.05.035

Yershov, E.D., 1991. Geocryological map of Russia and neighboring republics, 1:2,500,000 scale.

Žák, K., Richter, D.K., Filippi, M., Živor, R., Deininger, M., Mangini, A., Scholz, D., 2012. Coarsely crystalline cryogenic cave carbonate-a new archive to estimate the Last Glacial minimum permafrost depth in Central Europe. Clim. Past 8, 1821–1837. doi:10.5194/cp-8-1821-2012